On-orbit Optical Detection of Lethal Non-Trackable Debris; Ground Testing Summary

Andrew C. Nicholas, Joshua M. Wolf, Lee J. Kordella, Ted T. Finne, Charles M. Brown, Scott A. Budzien, Kenneth D. Marr, Christoph R. Englert

Naval Research Laboratory
Washington, DC 20375
UNITED STATES

Andrew.Nicholas@nrl.navy.mil

ABSTRACT

Objects in the size range of 0.1 mm to 3 cm are not currently trackable but have enough kinetic energy to have lethal consequences for spacecraft. The assessment of small orbital debris, potentially posing a risk to most space missions, requires the combination of a large sensor area and large time coverage. For example, a sensor with a time•area product of 3 m^2-years is considered sufficient to make a significant contribution to our understanding of the near-Earth small debris population. Deploying large sensors, however, is generally resource intensive, due to their size and weight. The lightsheet sensor concept, allows the creation of a "virtual witness plate", which is created without any supporting physical structure and therefore presents an attractive opportunity for the detection small debris anywhere between low Earth orbit and interplanetary space. This sensor project is called Lightsheet Anomaly Resolution And Debris Observation (LARADO). Recent technology maturation efforts in the laboratory have successfully detected small debris (1.6 mm diameter) moving at 6.38 km/s. NRL is building the NASA funded the LARADO instrument as a technology maturation effort for a flight demonstration on STPSat-7 in 2024. In this presentation, we will describe the LARADO instrument, present the laboratory data and analysis, and describe the instrument details for the STPSat-7 spacecraft slated for launch via the DoD Space Test Program in CY2024.

1.0 INTRODUCTION

The number of man-made debris objects orbiting Earth [1], or orbital debris, as seen in Fig. 1, is increasing at an alarming rate, resulting in the increased probability of degradation, damage, or destruction of operating spacecraft. In particular, small objects (10cm to 1 µm) in Low Earth Orbit (LEO) are of concern because they are abundant, difficult to track or even to detect on a routine basis, and have enough kinetic energy to damage spacecraft [2,3]. Fragmentation debris has created three, as annotated in Fig. 1, recent step increases in the number of objects related to: 1) the 2007 Chinese ASAT test, 2) the 2009 Iridium/COSMOS collision, and 3) the 2021 Russian ASAT test. Objects in the size range of several cm down to 0.1 mm are too small to be tracked effectively but have enough kinetic energy to cause anomalies or catastrophic damage to spacecraft. Small objects moving at orbital velocities pack enough kinetic energy do serious damage as illustrated in Fig. 2. We call this category of debris "lethal non-trackable". Due to the increasing debris population, it is reasonable to assume that improved capabilities for on-orbit damage attribution, in addition to increased capabilities to detect and track small objects are needed. In this paper we present an instrument to detect debris in this lethal non-trackable category and to help characterize such debris distributions.
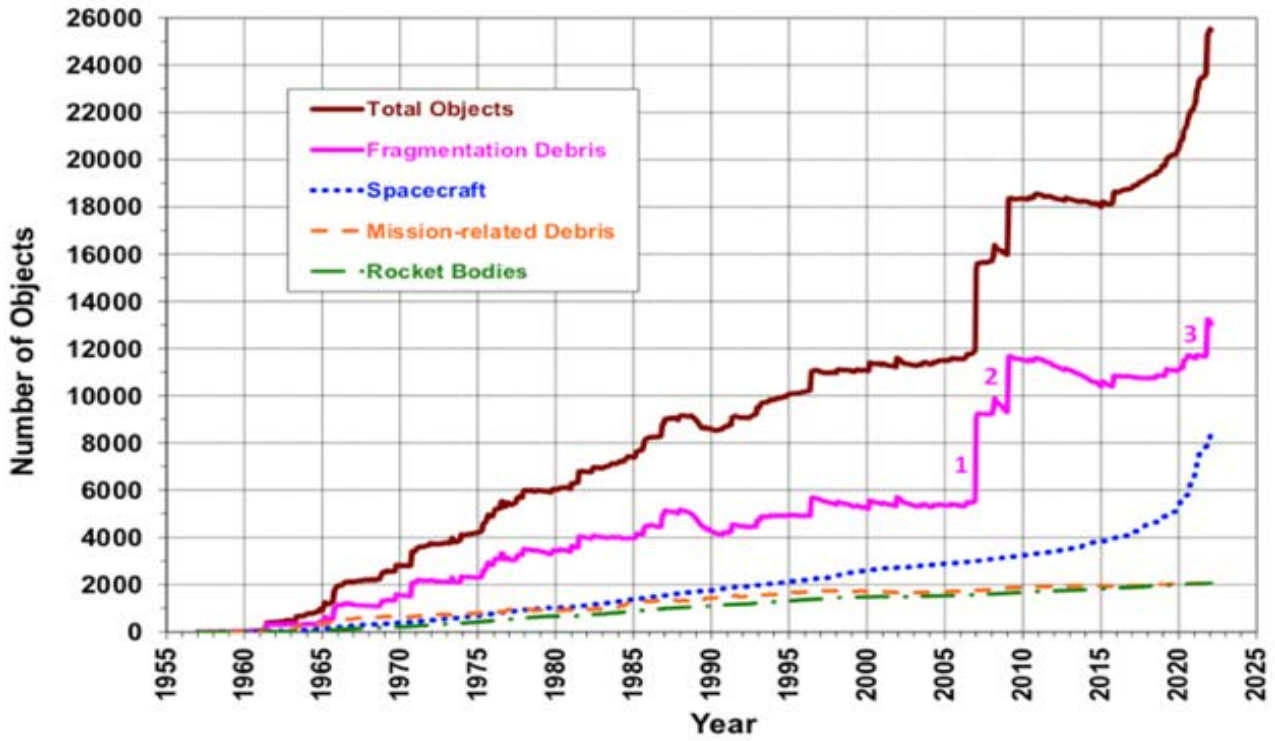
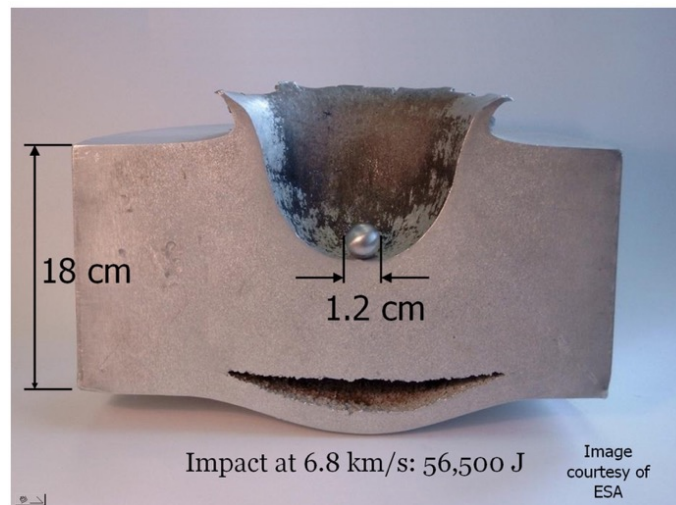**Figure 1. Historical count of cataloged space objects.**

Figure 2. Damage caused by a 1.2 cm diameter aluminum sphere striking an 18 cm thick plate of aluminum at 6.8 km/s. (Photo courtesy of ESA)

2.0 SENSOR CONCEPT

The LARADO sensor concept is based on creating a sheet of light in front of the host spacecraft and observing photons scattered by objects passing through the lightsheet. The lightsheet is created via a collimated light source that is connected to a diffusive optic, such as an axicon, Powell lens, or engineered diffuser. An optical lens coupled to a detector provides a method to monitor the scene. This system creates a virtual witness plate (VWP) for debris observations as seen in Fig. 3. The functional area of the virtual witness plate is scalable and defined by the components of the system: the power of the laser, the diffusive optic, the optics field of view (FOV) and aperture, and the detector sensitivity. The scalable nature of this instrument is unique in that it allows significant area coverage when compared with debris detection phenomenology that rely on impact observations. However, the data from these two methods are complementary as the impact method can also infer the mass density of the debris. A detailed description of the sensor concept and modeling is provided by Englert et al. [4] and Nicholas et al. [5], respectively. The DoD Space Test Program is developing the STPSat-7 spacecraft and mission that will host the LARADO sensor.
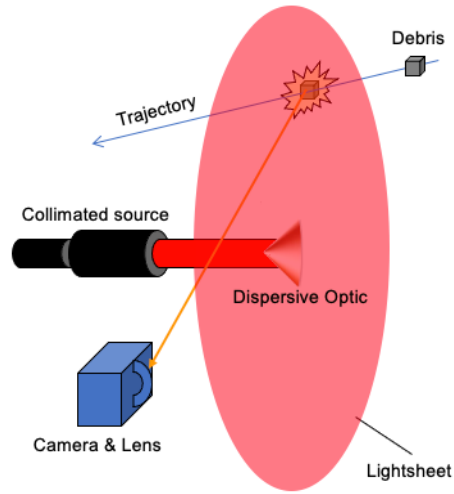

Figure 3. Representative components for the LARADO sensor concept depicting the creation of the lightsheet, or virtual witness plate, and debris passing through it scattering photons to the optical detection system.

3.0 LABORATORY TESTING AT NASA AMES

3.1 Chamber

The Ames Vertical Gun Range (AVGR) [6] is NASA's premiere hypervelocity impact facility for Planetary Geology and Geophysics research. The AVGR was brought on-line in 1966 to develop a better understanding of lunar surface geomorphology in support of the Apollo program and has since provided critical data that helped enable a variety of NASA missions including: Cassini, Deep Impact, LCROSS, Mars Odyssey, Stardust, and MER (Mars Exploration Rovers). With its unique hinged gun apparatus, the AVGR can vary the impact angle relative to the gravity vector (from horizontal to vertical). Targets are contained within a large impact chamber, as seen in Fig. 4, that can be evacuated to simulate impacts on an airless body or backfilled with air or various gases to simulate different environments. Typical impactors range in size from 1/16" to 1/4" (1.5875 to 6.35mm) in diameter, are of various composition (metal, plastic, glass, ceramic, mineral, etc.), and can be launched to speeds ranging from 0.5 to 7 km/s. A robust suite of high-speed video cameras (Vision Research and Shimadzu), lenses and lighting options can be positioned at many impact chamber window ports to capture impact events in great detail from a variety of perspectives.

The chamber has an internal diameter of 2.5 meters and is capable of reaching pressures as low as 0.5 torr at which all of our testing was performed. There is a large horizontal equipment platform that spans the inside of

the chamber with a one-meter diameter well in its center. An impact target material is placed inside of the well to stop the projectile. The chamber has four viewing ports on the top of the chamber, four on the side of the chamber, and two large windows on the side of the chamber. These viewing ports can be configured with any of the facility's high speeds camera to observe the event.

The gun assembly can be configured as a single-stage powder gun or a two-stage light gas gun. The powder gun uses a gunpowder charge to launch the projectile at speeds up to 2.5 km/s. The first stage of the light gas gun uses a gunpowder charge to drive a piston which compresses pure hydrogen in the second stage. A burst disk is located at the end of the second stage to hold back the projectile until a high burst pressure is reached. The light gas gun can fire the projectiles of speeds up to 6.5 km/s. The gun assembly can be inclined in increments of 15° to launch projectiles at angles from 0° to 90°. A thin diaphragm can be placed at the end of the gun barrel to delay the hydrogen gas from entering the chamber while allowing the solid projectile to punch through.

The projectile materials used include spherical aluminum, alumina, borosilicate, quartz, and Pyrex among others. Single projectile diameters ranged from 1/16" to 1/4". The projectiles are set into a sabot with four fingers that grip the projectiles inside the gun's chamber. The sabot gives the projectile a uniform shape to maximize the speed and stability of the projectile. After the gun is fired, the projectile and sabot move through the gun's barrel while spinning about the velocity axis. The spin causes the four fingers of the sabot to break apart and impact a cone shaped splitter which stops the sabot and allows only the projectile to continue through to the vacuum chamber.

Figure 4. Presents a photo of the AVGR facility, the blue structure is the vacuum chamber, the orange structure raises and lowers the gun. (Photo credit NRL/A. Nicholas).

3.2   Test Setup Geometry

The LARADO test support frame was constructed from 80/20 hardware with a 1/2" thick aluminum plate as its base. The setup includes: two cameras, a Ximea and a Prophesee (see below), and the laser sheet generation assembly. A cutaway model of the interior of the chamber is depicted in Fig. 5 with the LARADO test setup that includes the laser, lightsheet optics, and detectors mounted on the 80/20 aluminum test structure. A close-up view of the sensor support structure is presented as Fig. 6, clockwise from top-center the elements are the collimator/diffusive optic, the two cameras (Ximea CCD and Prophesee ganged in and out of page), and the nlight element-E06 laser module. The camera views are oriented 38.5° above the horizontal, other dimensions are provided in the figure. A plumb bob was hung along the AVGR firing axis to provide the projectile path during setup and camera focusing. A photo of the system during test setup is shown in Fig. 7. The lightsheet projects a horizontal fan of light that is parallel to the chamber floor, the projectiles enter from the top along the dotted yellow line. The photons that scatter of the projectile and to the camera are depicted by the dashed green line.

3.2.1 Laser

A survey of available laser and fiber optic combinations was made. Features sought were minimal size, weight, and power for future space flight opportunities. The laser must fit within the power, mass, and thermal budgets of a small spacecraft. In addition, spaceflight heritage was sought. Wavelengths compatible with COTS optics and sensors are also necessary. In the end, the nlight element™ E06 diode laser [7] operating at 793nm was chosen. This is a 30W CW laser that has spaceflight heritage from the ICESat-2 [8] and STPSat-5 HALO-net [9,10] missions. For the testing reported here the laser was operated at settings that produced 15W optical output.

3.2.2 The Lightsheet

The lasersheet assembly is composed of four components: an adjustable fiber collimator that collimates emitted laser light from a fiber optic cable, an adapter to mount the collimator, a diffusive optic that creates a fan-shaped sheet from the collimated laser light, and a 6-axis kinematic mount to position and orient components.
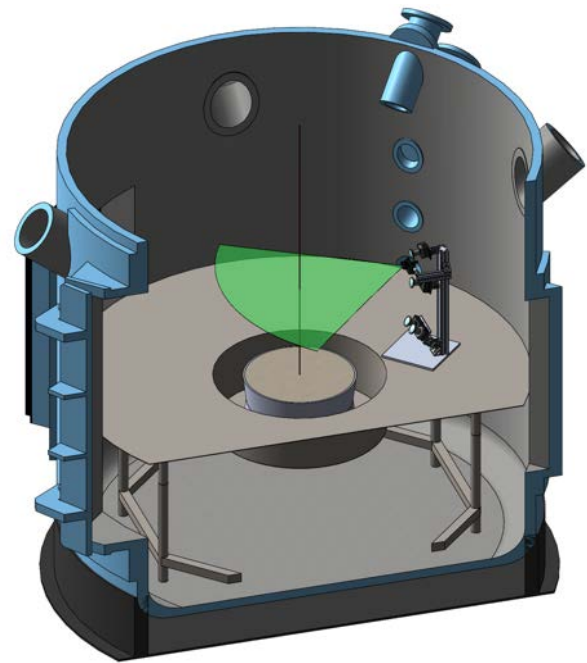

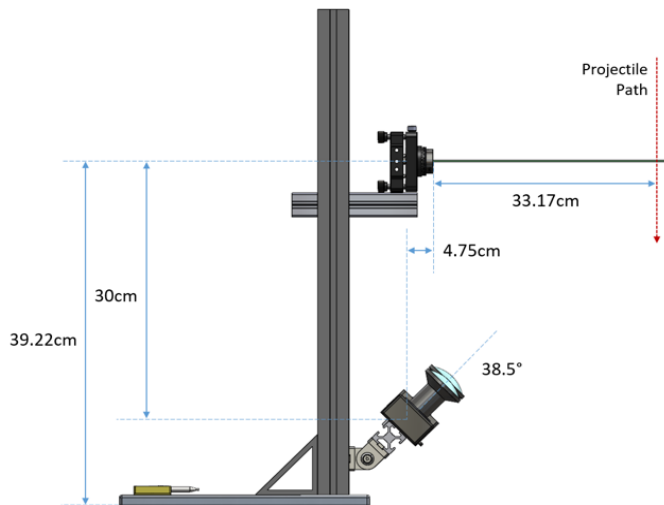**Figure 5. A visual representation of the AVGR chamber.**

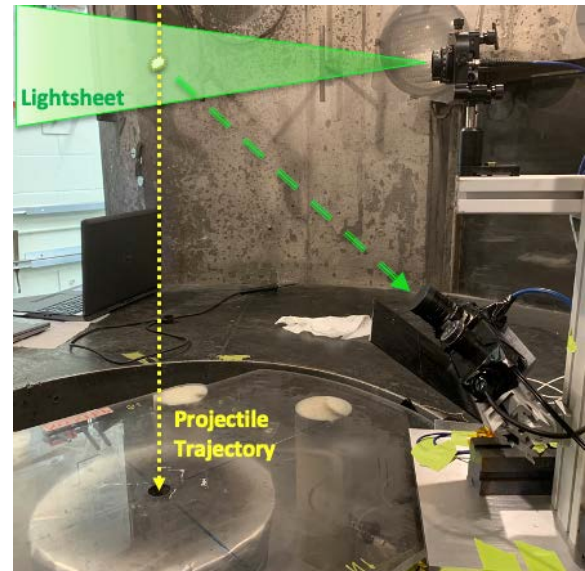**Figure 6. Test geometry inside the AVGR chamber.**

Figure 7. Annotated photograph of the LARADO test setup in the AVGR chamber.
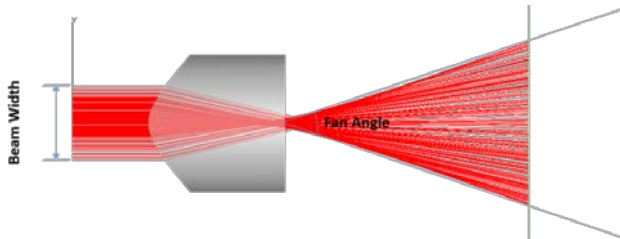
**Figure 8. Ray tracing of a collimated beam passing
through a Powell lens.**

The laser light travels through a 105-micron multimode step index fiber to the focal point of a 11mm focal length collimating lens producing a collimated circular beam. Thereafter, two methods of generating a sheet of laser light were employed. The first used an engineered diffuser [11] that generated a light sheet of 100° by 0.4° divergence. It was the easiest generator to mount and align, needing only a rotary stage to orient the light sheet in the desired plane. The engineered diffusers are an array of micro lenses generated by micro replication in a polymer. While they worked well at low power, the micro lenses and their plastic substrates melted at higher laser powers and at exposures of over 1 minute. More robust micro lens materials produced by reactive ion etching [12] are being developed for our space flight applications.

The second sheet generation method used a variation on a cylindrical lens called a Powell lens. It is an improvement on a simple cylindrical lens and can be figured to produce uniform light sheets based on the laser beam diameter and intensity distribution [13,14,15]. Being made of glass, the lens is able to survive the 30W beam in vacuum without convective cooling. In addition to a rotary stage, it requires a lens holder and X and Y centering adjusters. The front face is manually adjusted to be normal to the collimated laser beam. Due to the early failure of the plastic engineered diffuser, the Powell lens system was used for all subsequent shots at AVGR in this test. The present Powell lens is 8.9mm in diameter and is designed to produce a 75° fan beam for an input beam diameter of 4mm. Fig. 8 presents ray tracing results of the lightsheet generation system.

A collimator lens of 11mm focal length collects the light from the NA ~0.15 output of the fiber optic and produces a collimated beam with diameter of 4mm and a divergence of 0.55°. The Powell lens spreads it to 75° in the horizontal dimension while leaving the vertical divergence at 0.55° from the collimator.

3.2.3 Ximea Camera

One of the cameras chosen for the demonstration was a monochrome charge coupled device (CCD) progressive scanning camera manufactured by Ximea. The camera's model number is MD061MU-SY and is a part of Ximea's XiD family of USB3 cameras. The datasheet can be found online at: https://www.ximea.com/en/usb3-vision-camera/usb3-ccd-cameras-xid. The resolution of the camera is 2752 x 2202 pixels and can be cropped into a smaller region of interest (ROI) or pixel binned for faster readout speeds. It utilizes Sony's ICX814AL sensor chip which is 12.5mm by 10.0mm with each pixel within the sensor being 4.54μm. A photo of the camera is presented in Fig. 9.

**Figure 9. The Ximea XiD CCD
camera model MD061MU-SY.**

This camera uses C-mount lenses. The camera's dimensions are 60mm x 60mm x 37.2mm and has a mass of 320 grams without a lens attached. It has M4 mounting locations on the front, back, and bottom of the camera. The back of the camera can also couple to a heatsink to dissipate the camera's internal heat.

The camera output is capable of resolutions of 8, 10, 12, or 14 bits per pixel. The sensor can be split into 1, 2 or 4 sensor regions (TAPs) to increase the readout speed. Each TAP utilizes its own analog to digital convertor. Setting a region of interest (ROI) also can speed up the readout. A subset of the camera's pixels can be selected for readout by providing a width, height, x offset, and y offset of the desired region. When decreasing the number of horizontal rows being read out, the CCD can quickly skip over unwanted rows. Vertical ROI adjustments are completed on the software side and do not provide increased readout speed. Individual pixels can also be combined into super pixels using the binning process. Square pixel groups of up to 5x5 can be created with the individual pixels values in each group being summed or averaged.

3.2.4   Prophesee Neuromorphic Camera

 An event-based, or neuromorphic, camera [16] is based on a sensor that only records changes in brightness of the observed scene. Unlike conventional frame-based cameras, a neuromorphic camera does not capture image frames using a shutter, rather each pixel operates independently only reporting changes in brightness for that pixel as they occur. The camera's output, for each individual pixel, a 1 for an increase in brightness above a set

**Figure 10. How a neuromorphic camera works
compared to a traditional frame camera.**

threshold, a 0 for a decrease in brightness below an independently set threshold, or no output if the brightness remains unchanged. Each pixel responds asynchronously to changes in brightness as they occur [17]. A comparison between a reference brightness for each pixel from the last event and the current brightness is used to determine if an event occurred. If that brightness increased (or decreased) above (or below) a set threshold, an event is generated with a timestamp, pixel location, and polarity (increase or decrease, 1 or 0) [18]. The reference value for that pixel is then reset to the last observed brightness and the comparisons continue. Each pixel is capable of measuring illumination changes in a scene at high speeds (µs).
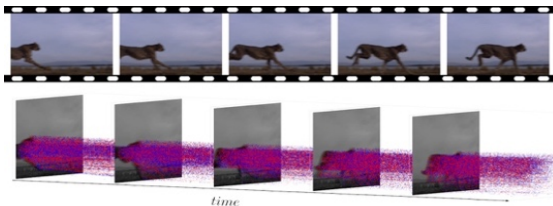
The use of a neuromorphic camera the orbital debris application has several advantages including high speed output, large dynamic range, and reduced data bandwidth. This technology is well-suited for fast impulsive event detection above a background scene as is expected with small orbital debris passing through the LARADO lightsheet at 8 to 15 km/s. In a traditional frame-based camera, such as the Ximea, a frame is collected over a set exposure period. For the AVGR testing the Ximea exposures were set to 40 ms. The debris spends about 1 ms in the lightsheet. This means that in the traditional frame camera, the signal of from the debris is exposed for a <1ms while the background of the scene is exposed 40 times longer.

The observations of a neuromorphic camera are depicted in Fig. 10 where the pink (increases in brightness) and blue (decreases) dots represent the continuous motion of a cheetah super imposed between frames from a traditional camera. The high-speed nature of a neuromorphic camera provides a tremendous advantage over the traditional frame-based cameras. However, due to the fact that the neuromorphic camera does not report the actual brightness it is limited in the amount of characterization of the debris (was it bright or dim?) it can measure. For our laboratory work the Prophesee 4.1 HD camera, based on the Sony MX636 1/2.5-type chip, was selected. This camera, shown in Fig. 11 has 1280 x 720, 4.86-micron pixel resolution and uses a USB 3 interface.

Figure 11. The Prophesee 4.1 HD neuromorphic camera.

3.2.5 View, Geometry & Lens Selection, FOV Coverages, Area Observed

Sections 3.2.3 and 3.2.4 describe the Ximea™ and Prophesee™ cameras. They have different sensor sizes and different area coverage requirements; thus, they require different focal length lenses.

While the AVGR target area could be confined to a few square inches, the lens selection was made to approximate an orbital viewing geometry requiring 60° or more to meet mission goals. Thus a 12.5 mm focal length lens was chosen for the Ximea camera and a 6 mm lens for the Prophesee. Likewise, large fan angles were selected for the Powell lenses and high powers employed for the laser to explore the coverage and light levels to be expected in space operations. To reduce background from out-of-band light, the Ximea camera used a Semrock 32-nm wide band filter centered at 794 nm while the Prophesee camera used an Andover 10-nm wide filter centered at 795 nm. The two cameras are mounted on a support tree made of 80/20 aluminum extrusions and are aligned and focused on the plumb bob hung at the target point. The focus and f/stop are manually adjusted to avoid saturation of the cameras at the laser intensity and frame rate employed. The intersection of the projected FOV with the lasersheet is shown in Fig. 12 for both the Ximea and the Prophesee cameras. The covered area is 0.476 m^2 and 0.371 m^2 respectively.
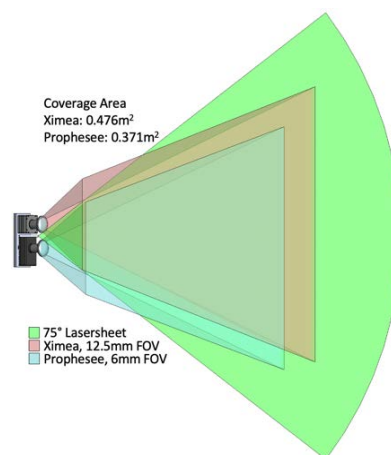
3.3 AVGR Data

3.3.1 Data Acquired

In total, twenty shots were taken over a test period of five days at the AVGR facility. Six shots were taken with the powder gun (PG), twelve shots were taken with the light gas gun (LGG), and additional two LGG shots were taken in an alternate

Figure 12. The projection of the Ximea and Prophesee FOV onto the 75º wide lightsheet.

Table 1. AVGR Shot Test Matrix.

Shot #	Gun	Size (in)	Size (mm)	Velocity (km/s)	Material
1	PG	1/4	6.35	0.61	Alumina
2	PG	1/4	6.35	2.32	Alumina
3	PG	3/16	4.7625	2.32	Alumina
4	PG	1/8	3.175	2.34	Alumina
5	PG	1/8	3.175	2.32	Al 6061
6	PG	1/8	3.175	2.32	Quartz
7	LGG 0.30 Cal	3/16	4.7625	4.5	Alumina
8	LGG 0.30 Cal	3/16	4.7625	N/A	Alumina
9	LGG 0.30 Cal	3/16	4.7625	N/A	Alumina
10	LGG 0.30 Cal	3/16	4.7625	5.84	Alumina
11	LGG 0.30 Cal	1/8	3.175	2.5	Alumina
12	LGG 0.30 Cal	1/8	3.175	3.11	Alumina
13	LGG 0.30 Cal	1/8	3.175	4.2	Aluminum
14	LGG 0.30 Cal	1/8	3.175	6.46	Alumina
15	LGG 0.22 Cal	1/16	1.5875	3.75	Alumina
16	LGG 0.22 Cal	1/16	1.5875	5.85	Aluminum
17	LGG 0.22 Cal	1/16	1.5875	5.26	Borosilicate
18	LGG 0.22 Cal	1/16	1.5875	6.38	Alumina
19*	LGG 0.30 Cal	1/4	6.35	5.07	Alumina
20*	LGG 0.30 Cal	3/16	4.76	5.87	Alumina

*Shots 19 & 20 were fired into simulated lunar regolith with cameras oriented to view ejecta

configuration for an application on the surface of the

moon. Table 1 provides the shot matrix providing gun information, particle size (diameter in both inches and mm), speed and material.

A photo of the actual projectile types and sizes is presented in Fig. 13, from left to right the first four are alumina, the next two are quartz and borosilicate glass, and the final two are aluminum.
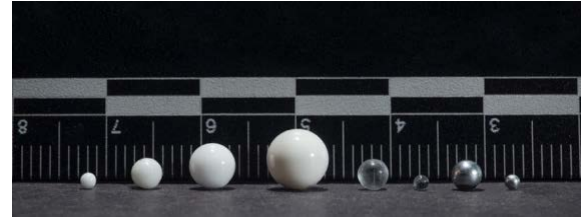
3.3.2 Data Analysis

The Ximea CCD camera images are processed to determine the frame in which the simulated debris crossing event occurs. Once that frame is identified an image difference between the event frame and the previous frame is calculated. This technique helps to reduce the background for the rest of the scene and make the impulsive debris event stand out. This process is presented in Fig. 14 for shot #3. The upper left image is a cropped (800 x 800) image of the event frame centered on the expected projectile crossing location in the bottom half of the image, chamber structure is clearly visible. The ¼" projectile is clearly seen at the center of this image. The image on the upper right is the last image acquired prior to the debris event. An image difference was calculated, Event Frame minus Previous Frame, and is presented in the lower left panel.

Figure 13. Photo of projectiles used during this testing at AMES. Photo credit NASA /JP Wiens.

Figure 14. Shot #3 image differencing process.

The difference image isolates the signal from the debris event. The lower right panel contains a zoomed (100 x 100) differenced image centered on the projectile.
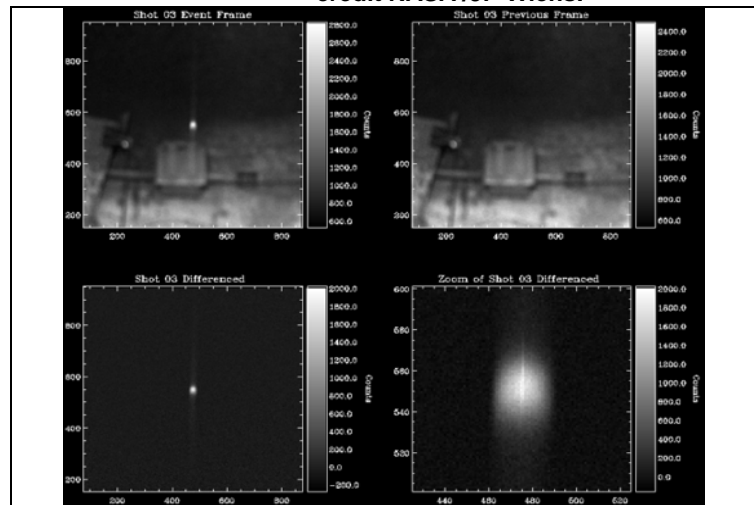
3.3.2.1 Ximea CCD Images

A series of differenced images from the Ximea camera are plotted in Fig. 15 as a set of images cropped to 800 x 800 pixels. Grayscale images represent alumina shots, green represent quartz or borosilicate glass, and blue images represent aluminum projectiles. In some of the images, gas from the gun creates a bright background. This is particularly evident in shots 7, 8, 10, 14, and 18. The exposure times were 40 ms, and the start of the exposure time is random with respect to the projectile crossing time, hence sometimes there is little gas accumulation in the frame with the event and other times there is a lot. It is a matter of timing, if the event occurs early in the 40ms interval, there will be a lot of background gas, and if late there will be less. Shots 8 and 9 were misfires by the LGG. Shot 10's image was swamped by gas from the LGG entering the scene and Shot 11 had no data due to a Ximea camera connection issue. A sequence of differenced images centered on the projectile and cropped to 100 x100 pixels is presented as Fig. 16. In both figures the projectiles are visible as are other particles consisting gunpowder from the PG shots and upward moving debris ejected from the impact of the projectile with the polyethylene backstop.
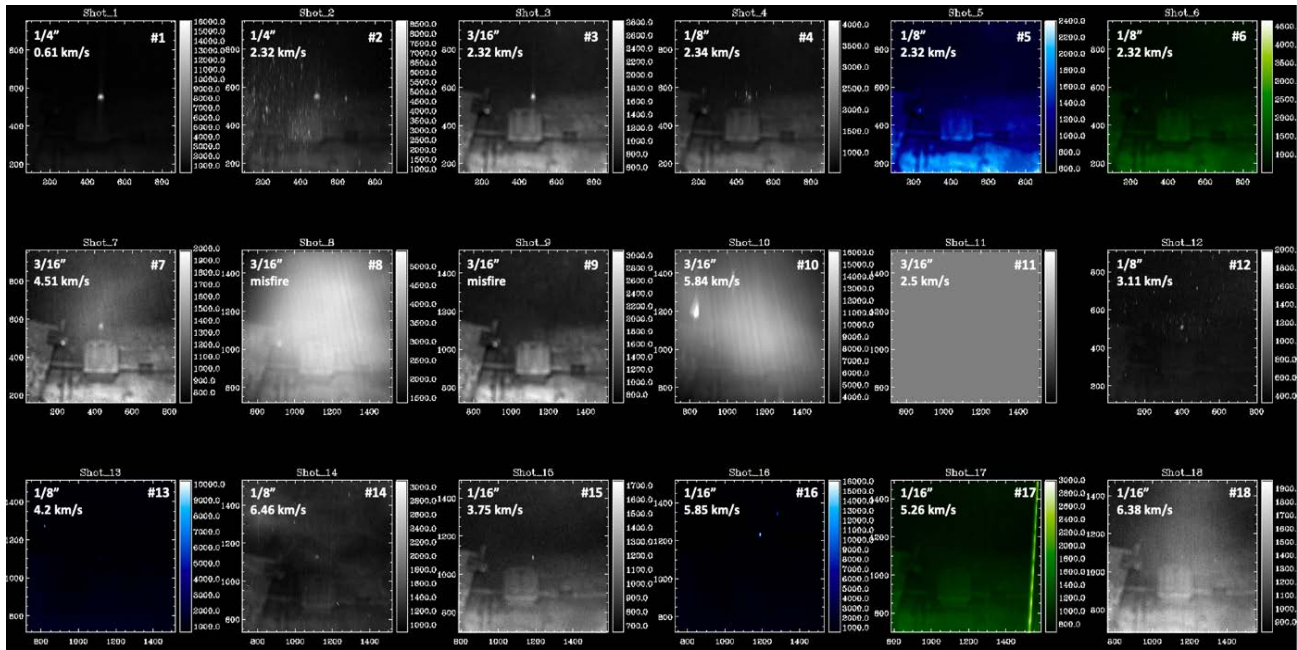
Figure 15.   Cropped (800 x 800) images from the Ximea camera for shots 1 through 18.
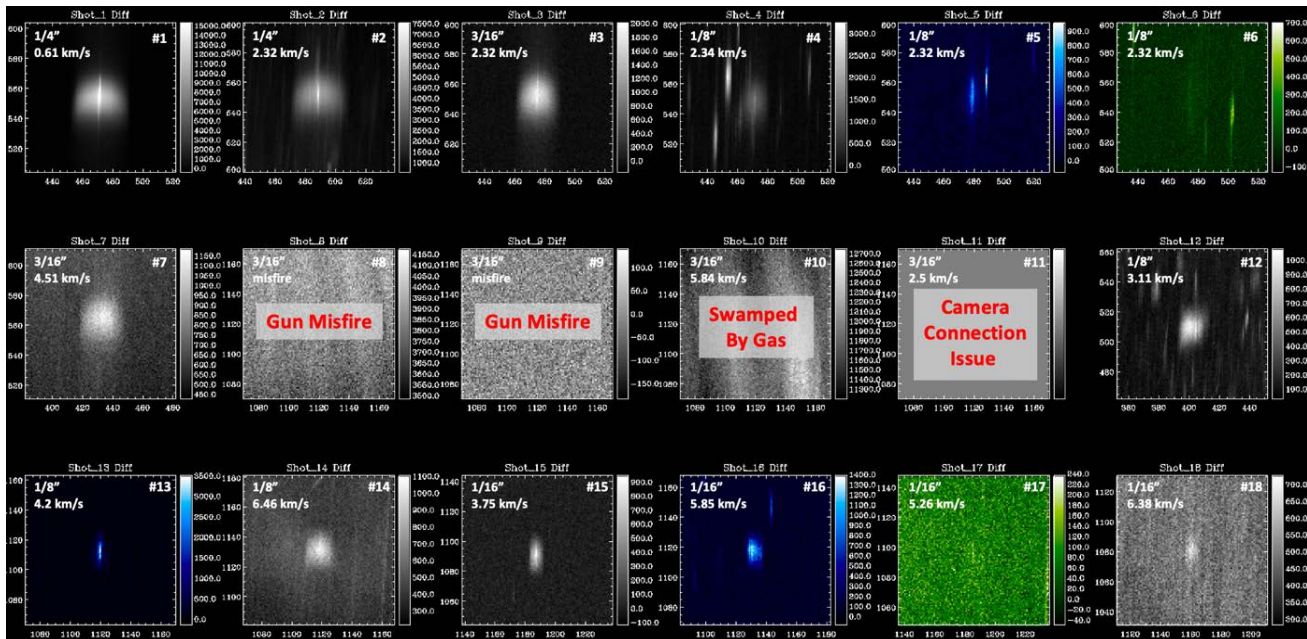

Figure 16.   Cropped (100 x 100) differenced images (event frame minus previous frame) from the
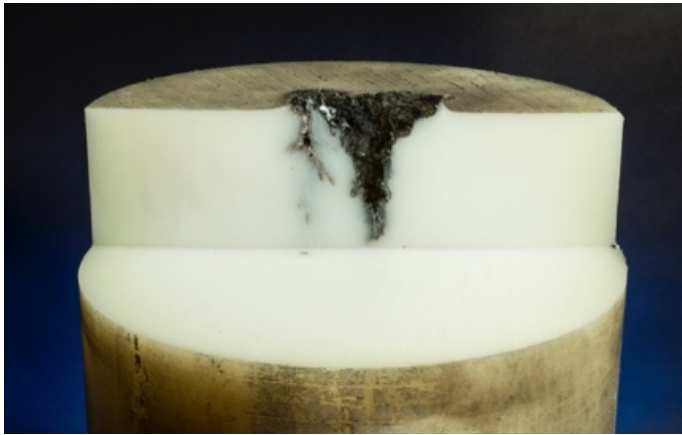Ximea camera for shots 1 through 18.

Figure 17.   A cross-section of one of the polyethylene backstops taken after multiple shots. Photo credit NASA /JP Wiens.

A cross-section of a polyethylene cylinder after several impacts is shown in Fig. 17. The ejecta moving upward and outward from the polyethylene cylinder is slower and thus they often provide more signal that the actual projectile. Signal levels expectedly decrease with increasing object speed and increase with increasing albedo; however, the different projectiles provide a variety of surfaces such that the observed signal of the projectile in the sheet can appear Lambertian, specular or a mix of the two. The alumina projectiles display a specular (especially evident under 3 km/s) and Lambertian response while the aluminum, quartz and borosilicate glass are mostly specular in response. Analysis of the pixel width of the observed responses confirm that computed spatial information is consistent with particle size for projectiles with Lambertian responses. For example, one can clearly see the expected relative spatial sizes of the alumina projectiles in shots 2 (1/4"), 7 (3/16"), 14 (1/8"), and 15 (1/16"). These relative spatial sizes are summarized in Table 2 and indicate that the observations are capturing the full width of the projectile. The measured scale for this setup is 0.16mm/pixel at the projectile's crossing point with the lightsheet. Detections of the aluminum projectiles in shots 5, 13 & 16 display a distinctively specular return. Both the quartz and borosilicate glass measurements exhibit dim specular (returns low albedo), however all shots (except for shot 10) were visible above the background, which at times can be excessive due to the test setup.

An analysis was performed on each differenced event frame to determine the peak counts in the event, the average background counts, and the total counts in the event. An example is provided for shot 15 in Fig. 18, where the dashed box represents the pixels summed for the event total. Table 3 presents a summary of this analysis for all shots.

Table 2. Ximea Spatial Size

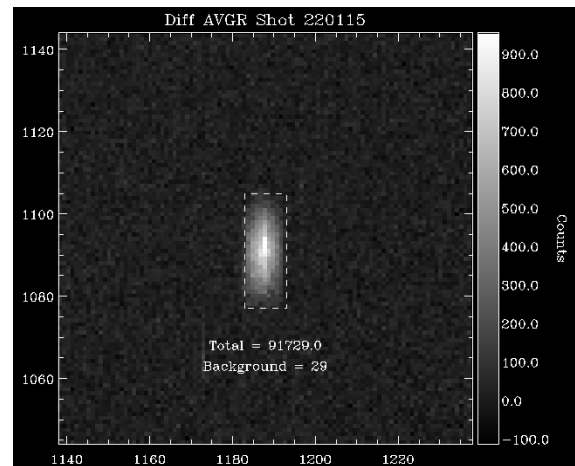| Shot #	Gun	Size (in)	Size (pix)	Ratio to Shot 2
2	PG	1/4	39	1.000
7	LGG	3/16	29	0.744
14	LGG	1/8	20	0.513
15	LGG	1/16	10	0.256

Figure 18.   A cross-section of one of the polyethylene backstops taken after multiple shots. Photo credit NASA /JP Wiens.

Table 3. Event Statistics

| Shot #	Peak	Sum in Event	Background	Material
1	15627	8279200	155	Alumina
2	7675	4325710	1115	Alumina
3	2054	919030	20	Alumina
4	1659	413298	122	Alumina
5	782	114307	75	Aluminum
6	170	29679	26	Quartz
7	1198	1099920	623	Alumina
8	N/A	N/A	N/A	Alumina
9	N/A	N/A	N/A	Alumina
10	N/A	N/A	N/A	Alumina
11	N/A	N/A	N/A	Alumina
12	1097	336087	162	Alumina
13	3577	178794	63	Aluminum
14	1122	427775	461	Alumina
15	967	91729	29	Alumina
16	1418	181506	108	Aluminum
17	242	27003	89	Borosilicate
18	735	130471	486	Alumina
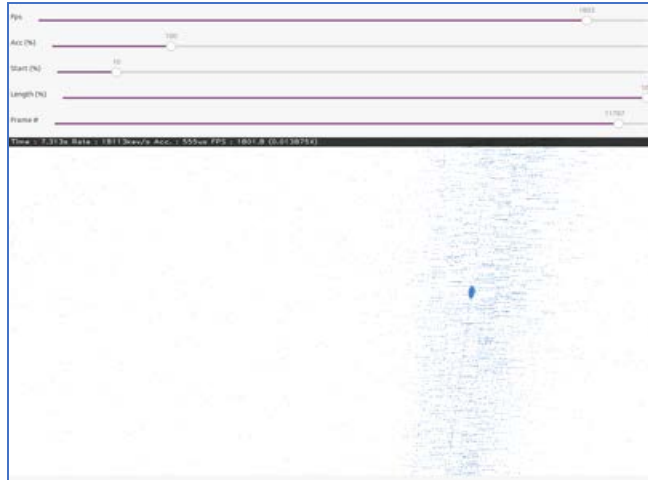
Figure 19. Event analysis of Shot 15, a 1/16" alumina projectile moving at 6.38 km/s. The projectile shines brightly as it passes through the laser sheet, and is entrained in a jet of its propellant gas.

3.3.2.1 Neuromorphic Data

The Prophesee neuromorphic camera was able to measure the projectiles crossing the laser sheet, although we had some trouble with the optical filter. Once removed and the stock 5mm lens fitted, we were able to capture data showing clear events crossing the lightsheet. An artificial image was created in Fig. 19 by displaying blue (black) dots represent pixels that increased (decreased) in brightness in a 100 μs slice of time (10,000 fps equivalent) during shot 18. A 1/16" dia. alumina projectile was captured moving at 6.38 km/s. These are promising results, further analysis and tuning of the neuromorphic camera's bias settings are planned for future research.

4.0 STPSAT-7 GEOMETRY

STPSat-7 is a small ESPA class spacecraft with the LARADO instrument components mounted on the zenith panel. Due to limited bandwidth on STPSat-7, we are unable to downlink all of the raw images from the LARADO sensor, therefore we designed LARADO with two cameras that view the lightsheet from different vantage points. One camera views the lightsheet from an isometric perspective and one camera views parallel to the lightsheet. The parallel camera FOV can be reduced to only view the width of the lasersheet reducing the amount of on-board memory and processing power required for event detection. When an event is detected, it will trigger the spacecraft to download data from both camera views. This technique significantly reduced the amount of data telemetered to the ground, allows the parallel view camera to operate at a faster cadence, reduces the complexity of the on-board processing, and provides a 2nd view to discriminate false positives that may appear in a single camera due to cosmic rays. A second trip to AMES to test the is discussed in a future paper. The STPSat-7 LARADO configuration is presented in Figure 20, the upper left panel showing the laser sheet (purple) mounted on the zenith face of the spacecraft near the ram side and the parallel camera FOV (blue). The lower left shows the parallel camera boresight view (dark blue) with the purple representing the laser sheet. The top right panel (ram direction is to the right) presents a view of the STPSat-7 starboard panel depicting the location of the zenith mounted isometric view camera and it's FOV (green). Area coverage of the lasersheet from each camera is depicted in Figure 21 and provided in Tables 4 and 5.
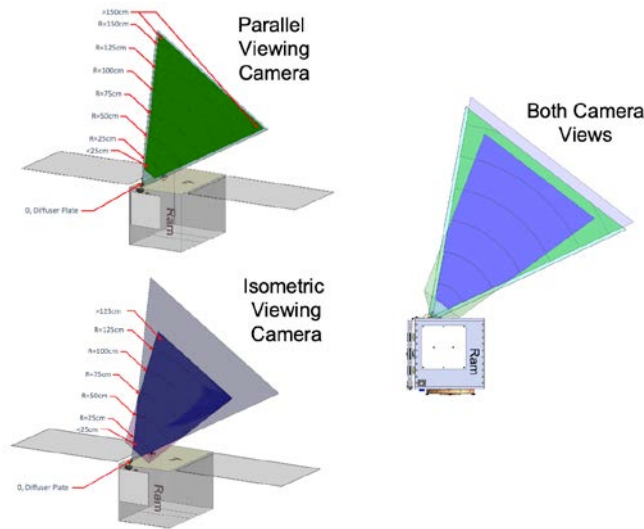
Figure 21. Configuration of lightsheet (purple) isometric (green) and parallel (blue) viewing cameras on STPSat-7.
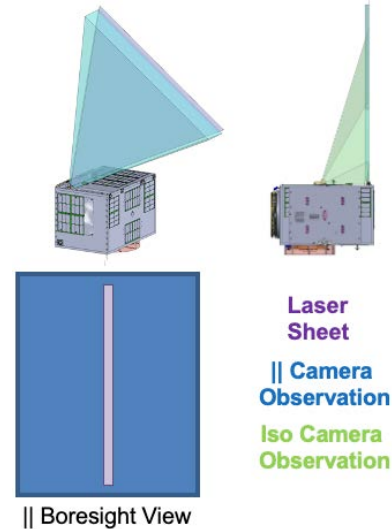

Figure 20. Configuration of lightsheet (purple) isometric (green) and parallel (blue) viewing cameras on STPSat-7.

Table 4. Parallel View Area Coverage

Radius (cm)	Sep (m)	Range/Radius (cm)	Area (m²)	∑ Area (m²)
<25	0.1962	<25	0.0226	0.0226
25	0.3174	25 – 50	0.0927	0.1153
50	0.5667	50 – 75	0.1527	0.268
75	0.8165	75 – 100	0.2127	0.4807
100	1.0663	100 –125	0.2727	0.7534
125	1.3163	125 – 150	0.2952	1.0486
150	1.5018	>150	0.0317	1.0803

Table 5. Isometric View Area Coverage

Radius (cm)	Sep (m)	Range/Radius (cm)	Area (m²)	∑ Area (m²)
<25	0.4512	<25	0.0254	0.0254
25	0.5114	25 – 50	0.0927	0.1181
50	0.6791	50 – 75	0.1513	0.2694
75	0.8865	75 – 100	0.1922	0.4616
100	1.1116	100 –125	0.2278	0.6894
125	1.3455	>125	0.1448	0.8342
>125	1.4476			

5.0   CONCLUSIONS

The lasersheet technique has been verified using small projectiles at near orbital velocities. Detections were made of single projectiles ranging from 1/4" to 1/16" (6.35 mm to 1.59 mm diameter) moving at speeds of 0.61 kms to 6.58 km/s. The fastest observation was a 1/16" (1.59 mm) alumina projectile moving at 6.58 km/s (week 2 shot 18). The smallest object detected was a 0.5 mm polyethylene sphere moving at 4.72 km/s (week 2 shot 23). This work has significantly increased the technological readiness level (TRL) of the sensing technique to TRL 6 on the NASA scale. Future plans include frame-by-frame analysis of the AVGR witness camera images, continued modelling of the events, optimization of the observational setup (goal of reducing the background gas in the event scene) and work on detection algorithms. The neuromorphic cameras seem well-suited for debris detection, however, even though current timelines restrict use on STPSat-7 potential use in future instruments exists and testing will continue. The LARADO instrument team is working towards the sensor Critical Design

Review (CDR) in the fall of 2022 for the instrument on the STPSat-7 spacecraft, an ESPA class vehicle that will have a 500 km circular orbit at an inclination of 60 degrees. Launch of STPSat-7 is slated for early-mid 2024.

6.0   AKNOWLEDGEMENTS

7.0   REFERENCES

[1]   NASA, Monthly number of objects in Earth orbit by type, Orbital Debris Quarterly News, Vol. 26 Iss. 1, March 2022.

[2]   R. Crowther, Space junk-protecting space for future generations, Science 296 (5571) (2002) 1241-1242.

[3]   National Aeronautics and Space Administration. "Process for Limiting Orbital Debris," NASA-STD-8719.14A (with Change 1), approved 2011-12-08.

[4]   C. Englert, et al., Optical Orbital Debris Spotter, Acta Astronautica, 104 (2014), 99-105.

[5]   A. C. Nicholas, C. R. Englert, C. M. Brown, T. T. Finne, K. D. Marr, C. R. Binz, L. M. Healy and S. T. Kindl. "Lightsheet Sensor for the Detection of Orbital Debris." International Conference on Orbital Debris, 6036, (2019).

[6]   J. Karcz , D. Bowling, C. Cornelison, A. Parrish, A. Perez, G. Raiche, and J.P. Wiens, "The AMES Vertical Gun Range", 47th Lunar and Planetary Science Conference, 2599, (2016).

[7]   nLight element e06 data sheet, https://www.nlight.net/semiconductor-lasers-products/element-e06-fiber-coupled-diode-laser-scph6

[8]   N. Sawruk, et. al., "Space certification and qualification programs for laser diode modules on the NASA ICESat-2 Mission," Proc. SPIE 8872, Lidar Remote Sensing for Environmental Monitoring XIV, 887204 (17 September 2013); doi: 10.1117/12.2026253.

[9]   D. Wayne, D. Obukhov, K. Brook, and M. Lovern, "A Large Aperture Modulated Retroreflector (MRR) for CubeSat Optical Communication," 28th Annual AIAA/USU Conference on Small Satellites," Logan, Utah (2014).

[10] D. Wayne, D. Obukhov, A. Phipps, M. Tran, K. Brook, and M. Lovern, "Design and Testing of a CubeSat-Sizes Retroreflector Payload," 29th Annual AIAA/USU Conference on Small Satellites, SSC15-P-40 Logan, Utah (2015).

[11] Laserline Optics Canada, Inc.

      https://www.laserlineoptics.com/store/product/powell-lens/ https://www.laserlineoptics.com/powell_primer.html

      https://www.laserlineoptics.com/powell_primer.html

[12] I. Powell, "Design of a laser beam line expander," APPLIED OPTICS, 26 3705 (1987).

[13] A. Bewsher, I. Powell, and W. Boland, "Design of single-element laser-beam shape projectors," Appl. Opt. 35, 1654-1658 (1996).

[14] H. Li; H. Liu; X. Ji; G. Li; L. Shi, (2017). "CIFAR10-DVS: An Event-Stream Dataset for Object Classification". Frontiers in Neuroscience. 11: 309. doi:10.3389/fnins.2017.00309. ISSN 1662-453X. PMC 5447775. PMID 28611582.

[15] P. Lichtsteiner; C. Posch; T. Delbruck, (February 2008). "A 128×128 120 dB 15μs Latency Asynchronous Temporal Contrast Vision Sensor" (PDF). IEEE Journal of Solid-State Circuits. 43(2): 566–576. Bibcode:2008IJSSC..43..566L. doi:10.1109/JSSC.2007.914337. ISSN 0018-9200. S2CID 6119048.

[16] C. Posch; D. Matolin; R. Wohlgenannt, (January 2011). "A QVGA 143 dB Dynamic Range Frame-Free PWM Image Sensor With Lossless Pixel-Level Video Compression and Time-Domain CDS". IEEE Journal of Solid-State Circuits. 46 (1): 259–275. Bibcode:2011IJSSC..46..259P. doi:10.1109/JSSC.2010.2085952. ISSN 0018-9200. S2CID 21317717.

[17] A. Nicholas; J. Wolf; L. Kordella; C. Brown; T. Finne; S. Budzien; K. Marr; C. Englert, "On-orbit Optical Detection of Lethal Non-Trackable Debris." Proceedings of the 73rd International Astronautical Congress, A6.1.71592, Paris France, (2022).